620 Vol. 43, No. 4 / April 2026 / Journal of the Optical Society of America B Research Article

Journal of the Optical Society of America B OPTICAL PHYSICS

Transit time corrections to the diffusion of atomic lattices

Alexander Pouliot,[1,*] Gehrig Carlse,[1] Eduardo Chomen Ramos,[1] Thomas Vacheresse,[1] Jaskaran Randhawa,[1] A. Kumarakrishnan,[1,4] Jacek Kłos,[2] and Eite Tiesinga[2,3]

[1]Department of Physics and Astronomy, York University, 4700 Keele St., Toronto, Ontario M3J 1P3, Canada
[2]Joint Quantum Institute, Department of Physics, University of Maryland, College Park, Maryland 20742, USA
[3]National Institute of Standards and Technology, Gaithersburg, Maryland 20899, USA
[4]akumar@yorku.ca
*alexpouliot@live.com

Received 13 October 2025; revised 6 February 2026; accepted 8 February 2026; posted 9 February 2026; published 2 March 2026

We present transit time corrections for the diffusive decay of an atomic ground-state population grating formed by spatially periodic optical pumping. We present results corresponding to two configurations, the first of which involves a population grating with a Gaussian envelope that is weakly probed using coherent scattering by a laser beam with a Gaussian spatial profile. The second configuration involves a population grating with a rectangular envelope that is weakly probed using coherent scattering by a laser beam with an idealized rectangular spatial profile of the same size. Recently, these corrections have been used to quantify systematic effects in measurements of Rb-inert gas diffusion coefficients near room temperature. Rubidium diffusion can be used to realize a quantum pressure sensor. © 2026 Optica Publishing Group. All rights, including for text and data mining (TDM), Artificial Intelligence (AI) training, and similar technologies, are reserved.

https://doi.org/10.1364/JOSAB.581437

1. INTRODUCTION

The effects of transit times of atoms either when passing through laser beams, moving from one laser beam to another, or between temporal laser pulses have received considerable interest in the fields of laser spectroscopy and precision metrology [1–5]. For example, a variety of coherent transient experiments that rely on photon echoes [6] require knowledge of state-prepared atoms that leave the interaction zone defined by excitation laser beams to estimate systematic effects. Another example involves atom trapping experiments, where the time-of-flight (ToF) distribution of cold atoms released from the trap is often of interest. Atom clouds are released from their traps, allowed to expand for a variable amount of time, and then imaged by fluorescence using resonant laser beams [7]. Knowledge of ToF distributions is also useful for calculating the transfer efficiencies of atoms from a low-vacuum chamber to an ultra-high-vacuum (UHV) chamber for Bose–Einstein condensate experiments [8]. Atom interferometers that measure atomic recoil [9], gravity [10,11], magnetic gradients [12], as well as velocimeters operating at room temperature [13] or with ultracold atoms [14] are all fundamentally limited in precision by the transit time of atoms.

Transit time corrections are also important for a variety of optical pumping experiments [15–19] and in coherent transient investigations of diffusion [20–22]. In this paper, we study the diffusive motion of localized, spatially periodic density profiles of dilute Rb samples in the presence of an inert buffer gas near ambient temperatures. The density profile, or lattice, is detected by coherently scattering light from a readout laser pulse applied after an initial excitation laser pulse, which created the profile. We show that the corrections depend on the spatial profile of the initial density distribution as well as on the readout laser beam. These corrections were crucial for reconciling our measurements of Rb $-$ X diffusion coefficients $D(T, p)$, as a function of temperature T and pressure p, with theoretical calculations [20,21]. These reconciliations have resolved a decades-long discrepancy between experiment and theory, and allowed determinations of the buffer gas pressure based on measurements of diffusion coefficients. We have proposed the realization of a quantum pressure sensor operating in the range 7000 Pa to 90,000 Pa based on this technique. Such a pressure sensor would be dependent on intrinsic atomic properties and immune to calibration drifts that affect electromechanical sensors.

We focus on the diffusion measurements in Refs. [20,21], in which we studied coherent light scattering from one-dimensional (1-D) periodic population distributions in trace Rb vapor on the order of 10^{-5} Pa in the presence of an inert buffer gas at a pressure that is at least six orders of magnitude larger than the Rb vapor pressure. We examine the corrections to the decay of such scattered signals due to the transit of a localized

spatial distribution of atoms probed by an optical field with a well-defined spatial profile.

The remainder of this paper is structured as follows: in Section 2, we describe the theoretical approach used to calculate the evolution of spatial population distributions. We review the case where there is no transit time correction in Section 3. In Section 4, we calculate the evolution of the population distribution when the initial distribution and the readout beam have two-dimensional Gaussian profiles with related width parameters. In Section 5, we study the evolution of the population distribution for an initial distribution and readout beam with the same rectangular cuboid spatial profile. Because of the complex spatial profile of the laser beam and the influence of saturation effects in optical pumping on the density profile of the population grating (discussed in Section 5), the experimental configurations realized in Refs. [20,21] lie somewhere between these two geometries. Therefore, we calculate the correction due to each model and adopt a conservative procedure to estimate the error. We describe the impact of these corrections in Section 6.

2. THEORETICAL APPROACH AND ASSUMPTIONS

We consider Rb-based diffusion experiments where the gases are at or near room temperature, buffer gas pressures are greater than 7000 Pa, and lattices have periods near 100 μm, which is much larger than the mean free path for Rb atoms scattering from buffer gas atoms or molecules [23]. Moreover, we can assume that the Rb atoms do not collide with each other during the measurement procedure. Under these conditions, the evolution of the Rb number density $\rho(\vec{r}, t)$ at position $\vec{r}$ and time t is described by the equation

$$\frac{\partial \rho(\vec{r}, t)}{\partial t} = D(T, p)\nabla^2 \rho(\vec{r}, t), \tag{1}$$

where the diffusion coefficient $D(T, p)$ is inversely proportional to pressure p.

A. Establishing an Initial Population Distribution

In Refs. [20,21], the initial Rb population distribution is established by two orthogonally polarized excitation pulses directed along $\vec{k}_1$ and $\vec{k}_2$ at a small angle θ on the order of 1 mrad, as shown in Fig. 1. These beams originate from a common laser and are focused through their respective AOMs using a common lens. Therefore, they have nearly identical spatial profiles, as any differences are due to variations in their respective collimating lenses. We choose $\vec{k}_1 + \vec{k}_2$ along our $\hat{z}$ axis, $\vec{k}_1 - \vec{k}_2$ is along our $\hat{x}$ axis, and $k = k_1 = k_2$. If the readout pulse, which has the same spatial profile as the excitation beam along $\vec{k}_2$, is turned on, the coherently scattered signal is produced along the phase-matched direction $\vec{k}_1$. In this case, the Rb population grating is formed along our $\hat{x}$ axis and has a wavevector $\kappa = k \sin\theta \approx k\theta$.

3. EVOLUTION WITHOUT TRANSIT TIME CORRECTIONS

The simplest periodic number density profile is created by assuming that the initial excitation laser pulses in Fig. 1 are

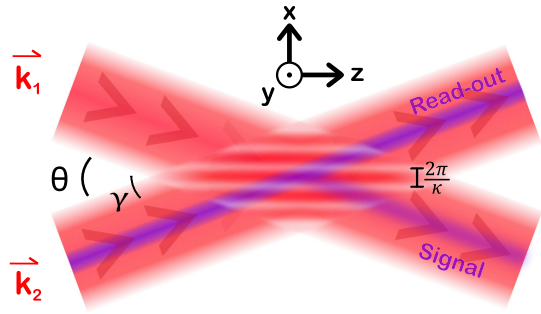


Fig. 1. Geometry of the excitation (red), readout (dark purple), and signal (light purple) optical laser beams in the experiments. The two pulsed excitation beams with wavevectors $\vec{k}_1$ and $\vec{k}_2$, respectively, are aligned with a relative angle of θ in the xz plane. Both beams have wavenumber k. A periodic Rb population distribution along the x axis (white/red interference pattern) with a period of $2\pi/\kappa$, where $\kappa = k \sin\theta$, forms in the overlapping region of the excitation lasers. The readout laser is applied at a later time with wavevector $\vec{k}_2$. For later use, we indicate angle $\gamma = \theta/2$ in the xz plane.

plane waves, and the population distribution, therefore, extends throughout all space. The number density profile at time $t = 0$ is then a one-dimensional sinusoidal function with wavenumber κ along the direction $\hat{x}$ given by

$$\rho_{\mathrm{pw}}(\vec{r}, t = 0) = \rho_0 + \rho_{\mathrm{A}} \cos(\kappa x). \tag{2}$$

Here, $\vec{r} = x\hat{x} + y\hat{y} + z\hat{z}$, where $\hat{x}$, $\hat{y}$, and $\hat{z}$ form an orthonormal set of unit vectors. Furthermore, ρ_0 and ρ_{A} are the positive mean number density and lattice amplitude, respectively. The choice of the phase of the lattice relative to the origin $\vec{x} = \vec{0}$ and orientation along $\hat{x}$ is arbitrary. We also assume $|\rho_{\mathrm{A}}| < \rho_0$.

A. Time Evolution of a Plane-Wave Number Density Distribution

The time evolution of the number density distribution in Eq. (2) is governed by Eq. (1). Therefore, the $t > 0$ solution is given by

$$\rho_{\mathrm{pw}}(\vec{r}, t) = \rho_0 + \rho_{\mathrm{A}} e^{-D\kappa^2 t} \cos(\kappa x). \tag{3}$$

Here, we have omitted the arguments of the diffusion coefficient for clarity. Equation (3) predicts an exponential reduction in the lattice amplitude with a time constant $\tau = 1/(D\kappa^2)$ without a change in the lattice period, which is visualized in Fig. 2. Measurements of τ and κ can then be used to find D. Our choices for D and κ in the simulation presented in Fig. 2 are typical for Rb diffusion in inert buffer gases at atmospheric pressure and ambient temperatures, the relevant optical transition frequency of Rb, and the small angle between the two excitation laser beams.

B. Bragg-Like Scattering from the Plane-Wave Number Distribution

The coherent optical field of the read-out pulse, with wavenumber k, is then applied at some later time. It propagates in the xz plane with an angle γ relative to the positive $\hat{z}$ direction. Coherent scattering of this field by the Rb atoms will be sharply peaked in a single direction. This direction is set by the Bragg or phase-matching condition for constructive interference given

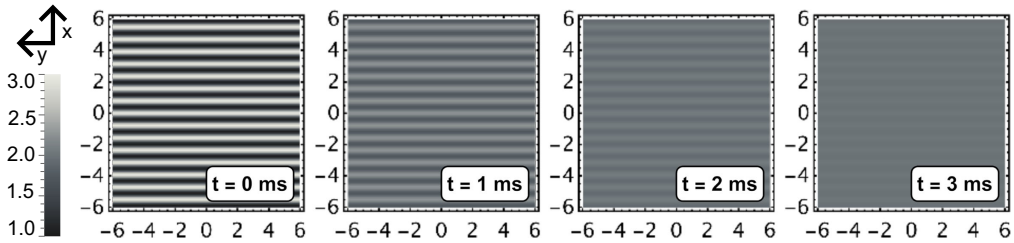


Fig. 2. Snapshots of the lattice amplitude of a plane-wave Rb number density distribution at four times during and after the excitation pulses. The lattice wavenumber and diffusion coefficient are 8 mm^{-1} and 20 mm^2/ms, respectively. The panels show the amplitude in the xy plane with lengths in units of mm. The color scale indicates the number density distribution with $\rho_0 = 2$ and $\rho_A = 1$ in arbitrary units. The orientations of the x and y axes of the panels are shown in the upper left corner of the figure.

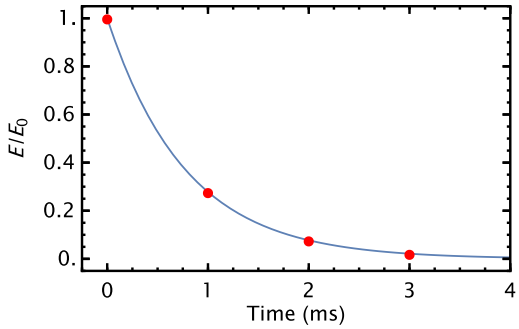


Fig. 3. Scattered electric field amplitude E from a plane wave Rb population distribution as a function of time. This curve is based on the same values for ρ_A, ρ_0, κ, and D as used to generate Fig. 2. The times of each snapshot in Fig. 2 are highlighted by red dots.

by [23,24]

$$m\frac{2\pi}{k} = 2\frac{2\pi}{\kappa}\sin\gamma\,, \tag{4}$$

where m is an integer. We choose the angle γ such that this condition is satisfied for $m = 1$. The direction of this signal or the scattered light is shown in Fig. 1.

The experiments use detectors that are aligned in such a manner that they collect only the coherently scattered light. In fact, we use a heterodyne detection system that is sensitive to the amplitude of the scattered electric field $E(t)$. The amplitude of this electric field is proportional to the amplitude of the Fourier component of the spatially periodic gratings in the populations of the magnetic sublevels m_F of the electronic ground state [20,24]. Here, the quantization axis for the m_F sublevels is along the lattice direction $\vec{k}_1 - \vec{k}_2$. For the plane wave case, the time dependence of the $\kappa\hat{x}$ Fourier component can be found by inspecting Eq. (3), resulting in a scattered signal of the form

$$E(t) = E_0 e^{-D\kappa^2 t}\,, \tag{5}$$

where E_0 is the electric field amplitude at time $t = 0$. This decay is shown in Fig. 3 for the same parameters as in Fig. 2.

4. GAUSSIAN DISTRIBUTION OF POPULATIONS AND READOUT WITH GAUSSIAN SPATIAL PROFILE

Our first attempt at a more realistic treatment of the experiments, in accordance with the geometrical constraints in Fig. 1, will assume that the excitation and readout beams are Gaussian laser beams that have the same two-dimensional Gaussian intensity profile in the xy plane and have an intensity profile that is independent of z along $\hat{z}$. Here, we have relied on observations that, in practice, the Rayleigh ranges of the beams are significantly longer than their beam waists and that we can ignore the effects due to the small angle θ between the excitation beams relative to the z axis. In fact, in our experiments, the Rayleigh ranges are 20 times longer than the length of the glass cell containing our inert buffer gases and Rb atoms. Consequently, the Rb transit times along the $\hat{x}$ and $\hat{y}$ directions will be much smaller than those for atoms reaching the vapor cell windows along $\hat{z}$.

The amplitude of the sinusoidal contribution to the initial population distribution $\rho_G(\vec{r}, 0)$ is proportional to the intensity profile of the excitation beams for low laser intensities. Since the measured signal is proportional to the scattered electric field (and not to the intensity) and the readout beam has the same spatial profile as the excitation beams, the $1/e$ widths of the initial population distribution of Rb and the electric field amplitude of the readout beam will differ by a factor of $\sqrt{2}$. We allow the $1/e$ widths to differ along the x and y axes in order to account for the asymmetric beam profile measured in the experiment [21]. The $1/e$ widths of the electric field will be denoted by lengths a and b, respectively. Therefore, we write the electric field amplitude of the readout beam as

$$E_{RO}(\vec{r}) = E_{RO}(\vec{0})e^{-(x/a)^2-(y/b)^2}\,, \tag{6}$$

where $E_{RO}(\vec{0})$ is the electric field strength at the center of the beam profile, and the initial population distribution as

$$\rho_G(\vec{r}, 0) = \rho_0 + \rho_A e^{-2(x/a)^2-2(y/b)^2}\cos(\kappa x)\,. \tag{7}$$

This expression represents the lattice amplitude ρ_A, as defined in Eq. (2), multiplied by the intensity profile.

A. Time Evolution of Gaussian Population Distribution

Unlike in Section 3, the more complicated form of the initial density distribution in Eq. (7) forces us to employ the general solution to Eq. (1). We express this general solution in terms of the 3-D Fourier transform $P(\vec{q})$ of $\rho(\vec{r}, 0)$ as

$$\rho(\vec{r}, t) = \frac{1}{(2\pi)^3}\int \mathrm{d}^3q\; P(\vec{q})e^{i\vec{q}\cdot\vec{r}}e^{-q^2Dt}\,, \tag{8}$$

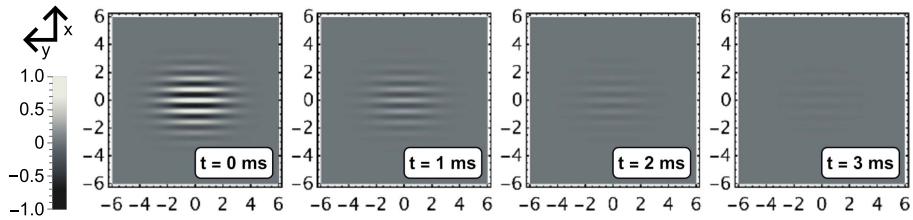


Fig. 4. Snapshots of the lattice amplitude in the xy plane given by the term proportional to ρ_A in Eq. (10) for an initial Gaussian population distribution. We used $\kappa = 8\ \mathrm{mm}^{-1}$, $D = 0.2\ \mathrm{cm}^2/\mathrm{s}$ as well as $a = 2.5$ mm and $b = 3$ mm. The horizontal and vertical axes in the snapshots show lengths in mm and correspond to our $\hat{x}$ and $\hat{y}$ directions, respectively. The color scale indicates the lattice amplitude with $\rho_A = 1$ in arbitrary units. The orientations of the x and y axes of the panels are shown in the upper left corner of the figure.

where the wavenumber vector $\vec{q} = q_x\hat{x} + q_y\hat{y} + q_z\hat{z}$. For the Gaussian Rb number density profile in Eq. (7), $P(\vec{q})$ is

$$P_G(\vec{q}) = (2\pi)^3 \left\{ \rho_0 \delta(\vec{q}) + \frac{ab}{16\pi}\rho_A e^{-a^2(q_x+\kappa)^2/8}\left(1 + e^{a^2\kappa q_x/2}\right) \times e^{-b^2 q_y^2/8}\delta(q_z) \right\}, \tag{9}$$

where $\delta(q_z)$ and $\delta(\vec{q})$ are the one- and three-dimensional Dirac delta functions, respectively, resulting in the solution

$$\rho_G(\vec{r}, t) = \rho_0 + \frac{ab}{\sqrt{A(t)B(t)}} e^{-\kappa^2 Dta^2/A(t)}\rho_A \times \cos(\kappa x a^2/A(t)) e^{-2x^2/A(t) - 2y^2/B(t)} \tag{10}$$

with time-dependent areas $A(t) = a^2 + 8Dt$ and $B(t) = b^2 + 8Dt$.

The quantity $\rho_G(\vec{r}, t) - \rho_0$ based on Eq. (10) is visualized in Fig. 4 for typical parameter values of our systems. We observe that the lattice period along the $\hat{x}$ axis and the widths of the spatial Gaussians are increasing as a function of time t, first slowly and then linearly for longer times. The amplitude of the number density distribution decreases, first exponentially but then slowly as $1/t$ for longer times t. In contrast, the amplitude of the number density distribution decreases exponentially for all times in the plane wave case.

B. Scattering of a Gaussian Readout Field from an Expanding Gaussian Rb Lattice

As in Section 3, our observed signal will be proportional to the $\kappa\hat{x}$ Fourier component of the Rb population distribution. However, unlike in Section 3, however, only the portion of the Rb number distribution that is illuminated by the readout beam produces coherently scattered light. So, to find the time dependence of the scattered field, we take the product of $E_{RO}(\vec{r})$ and $\rho_G(\vec{r}, t)$ and then find its Fourier component at $\kappa\hat{x}$. The result is

$$E_G(t) \propto \int d^3r\ \rho_G(\vec{r}, t) E_{RO}(\vec{r}) e^{-i\kappa x}, \tag{11}$$

which can be solved using

$$\int_{-\infty}^{\infty} dx e^{-(x/s)^2 - ikx} = \sqrt{\pi} s\, e^{-s^2k^2/4}$$

to obtain the scattered electric field as a function of time. It is given by

$$E_G(t) \propto E_{RO}(\vec{0})\rho_0 \pi ab L e^{-a^2\kappa^2/4} + E_{RO}(\vec{0})\rho_A \pi ab L \frac{ab}{\sqrt{\mathcal{A}(t)\mathcal{B}(t)}} e^{-\kappa^2 Dta^2/A(t)} \times e^{-a^2\kappa^2(1+a^4/A^2(t))A(t)/4\mathcal{A}(t)} \cosh\left(a^4\kappa^2/2\mathcal{A}(t)\right), \tag{12}$$

where areas $\mathcal{A}(t) = 3a^2 + 8Dt = A(t) + 2a^2$, $\mathcal{B}(t) = 3b^2 + 8Dt = B(t) + 2b^2$, and length L is the size of the glass cell along the $\hat{z}$ direction. This result in Eq. (12) represents a more accurate version of Eq. (22) in Ref. [21]. Nevertheless, the expressions are similar enough to produce the same transit time corrections.

For early times when $Dt \ll a^2$ and assuming that $a \approx b$, $a\kappa \gg 1$ has several periods over the beam radius a, and $\rho_0 \exp(-a^2\kappa^2/4)$, the time-independent background signal is $\ll \rho_A/6$, so that

$$E_G(t) \propto \frac{1}{6}\pi ab L E_{RO}(\vec{0})\rho_A e^{-\kappa^2 Dt} \times \left(1 + c_1\frac{Dt}{a^2} + c_2\frac{D^2t^2}{a^4} + O(D^3t^3/a^6)\right) \tag{13}$$

with negative

$$c_1 = -\frac{4}{3}\left(1 + \frac{a^2}{b^2}\right) \tag{14}$$

and positive

$$c_2 = \frac{8}{3}(\kappa a)^2 + 2 + \frac{16}{9}\frac{a^2}{b^2} + 2\frac{a^4}{b^4}, \tag{15}$$

resulting in a function that has the same short-time dependence as in the plane-wave case, i.e., $e^{-\kappa^2 Dt}$. Here, the symbol O represents the big O notation. For typical values of a, b, κ, and D, the term proportional to ρ_A in Eq. (12) will be many orders of magnitude larger than that from ρ_0 and $a\kappa \gg 1$. This observation agrees with the intuition that the periodic component of the density distribution will have a much greater impact than the constant offset component.

Figure 5 shows the ratio of Eqs. (12) and (5) obtained in the plane-wave case as a function of time, normalizing the electric

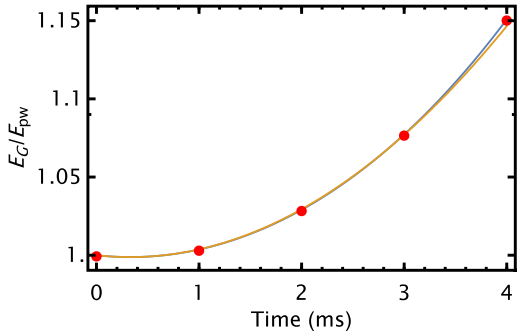


Fig. 5. Ratio of reflected electric fields from the plane-wave distribution E_{pw} and the Gaussian distribution with a Gaussian readout E_G as described by Eq. (12) as a function of time (blue). The quadratic approximation to this ratio, as shown in the parentheses of Eq. (13) (orange). All curves use the beam shape and diffusion parameters of Fig. 4. The electric fields have been normalized to have the same value at $t = 0$. The four left-most red points represent the times of the snapshots in Figs. 2 and 4.

fields to have the same value at $t = 0$. Figure 5 also shows the ratio of the quadratic approximation in Eq. (13) to Eq. (5) in the plane-wave case. The approximation is in close agreement with the other curve for the timescales typical of the diffusion measurements. Formally, we are in the regime $a \sim b$, $Dt \ll a^2$, and $Dt \gg 1/\kappa^2$ for the largest time shown in Fig. 5, consistent with the requirements for the validity of Eq. (13).

Although the deviation from the plane-wave case is as high as 15% for the time scale shown, this amounts to a modest correction to the diffusion coefficient. Nevertheless, it is statistically significant in precise determinations of $D(T, p)$ [21].

5. RECTANGULAR POPULATION DISTRIBUTION AND READOUT WITH RECTANGULAR SPATIAL PROFILE

The Gaussian population envelope assumed in Section 4 is not accurate for typical operating parameters due to saturation of optical pumping among the hyperfine states F, m_F of the electronic ground state of Rb at high excitation laser intensities. Typically, these lasers are tuned to the $5s$ to $5p$ electronic transition of the ^{85}Rb isotope. Simulations of optical pumping, following the procedures described in Ref. [25] based on [26] and shown in Fig. 6, demonstrate that most of the population is in hyperfine states with a grating envelope that has developed a top-hat shape. The width of this rectangle depends on the power of the excitation lasers as well as the pressure of the buffer gas.

We will now carry out calculations of transit-time corrections, assuming an initial rectangular lattice envelope with spatial dimensions α and β along the x and y axes, respectively. This is given by

$$\rho_{\text{rect}}(\vec{r}, 0) = \rho_0 + \begin{cases} \rho_A \cos(\kappa x) & \text{if } |x| \le \alpha/2 \;\&\; |y| \le \beta/2 \\ 0 & \text{otherwise} \end{cases}. \tag{16}$$

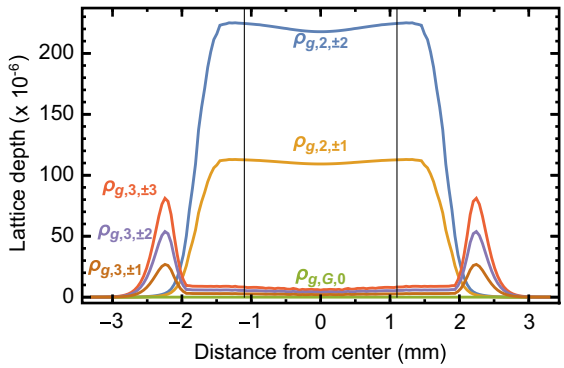


Fig. 6. Spatial dependence of the population for each F, m_F magnetic sublevel of the electronic ground state of ^{85}Rb along $\hat{x}$ with $y = z = 0$, i.e., the lattice depth or amplitude for each sublevel, obtained by rate equation simulations assuming Gaussian excitation pulses. The lattice depth is expressed as the deviation from equally populated Rb ground states as a fraction of the total Rb population. The black vertical lines indicate the $1/e$ radius of 1.1 mm of the electric field of the excitation lasers. We have used typical pulse and buffer gas parameters used in our experiments (50 μs pulse length, 70 mW total power, and 26,700 Pa of N_2 buffer gas).

A. Time Evolution of Rectangular Distribution

Using the same procedure as Section 4, we first find $P_{\text{rect}}(\vec{q})$ from the Fourier transform of $\rho_{\text{rect}}(\vec{r}, 0)$ to be

$$P_{\text{rect}}(\vec{q}) = (2\pi)^3 \left\{ \rho_0 \delta(\vec{q}) + \rho_A \frac{\alpha\beta}{8\pi^2} \left\{ \text{sinc}\left(\frac{[q_x + \kappa]\alpha}{2}\right) + \text{sinc}\left(\frac{[q_x - \kappa]\alpha}{2}\right) \right\} \text{sinc}\left(\frac{q_y \beta}{2}\right) \delta(q_z) \right\}. \tag{17}$$

Here, $\text{sinc}(z) = \sin(z)/z$. We then proceed to derive the time-dependent $\rho_{\text{rect}}(\vec{r}, t)$ and obtain

$$\rho_{\text{rect}}(\vec{r}, t) = \rho_0 + \frac{1}{4}\rho_A e^{-\kappa^2 Dt} \left(\text{erf}\left([y + \beta/2]/\sqrt{4Dt}\right) - \text{erf}\left([y - \beta/2]/\sqrt{4Dt}\right) \right) \times \text{Re}\left\{ e^{i\kappa x} \left[\text{erf}\left(\frac{x + \alpha/2}{\sqrt{4Dt}} + i\kappa\sqrt{Dt} \right) - \text{erf}\left(\frac{x - \alpha/2}{\sqrt{4Dt}} + i\kappa\sqrt{Dt} \right) \right] \right\}, \tag{18}$$

where $\text{erf}(z)$ is the error function with $\text{erf}(-z) = -\text{erf}(z)$ and $\text{erf}(x) \to \pm(1 - e^{-x^2}/\sqrt{\pi}x)$ for real $x \to \pm\infty$, respectively, based on Chapter 7 of Ref. [27], and we used Ref. [28] to perform the integrals. Equation (18) is even in both x and y.

The predictions of Eq. (18) are visualized in Fig. 7. We again observe that the amplitude of the sinusoidal pattern decays over time with limited expansion in the x and y directions.

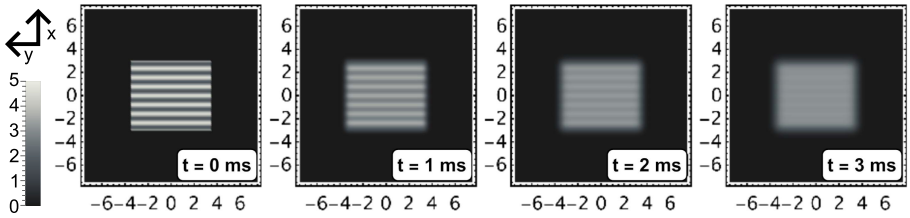


Fig. 7. Snapshots of the Rb lattice amplitude in the xy plane for an initial rectangular population distribution at times $t = 0, 1, 2, 3$ ms. The lattice wavenumber is 8 mm^{-1}, $\alpha = 6$ mm, $\beta = 7$ mm, and the diffusion coefficient is 0.2 cm^2/s. Lengths are in units of mm, and the color scale indicates the population in arbitrary units. The orientations of the x and y axes of the panels are shown in the upper left corner of the figure.

B. Scattering of a Rectangular Readout Field from an Expanding Rectangular Rb Lattice

The spatial profile of an idealized rectangular readout beam with dimensions α and β along $\hat{x}$ and $\hat{y}$, respectively, is given by

$$E_{\mathrm{RO}}(\vec{r}) = E_{\mathrm{RO}}(\vec{0}), \tag{19}$$

when $|x| \le \alpha/2$, $|y| \le \beta/2$, and $E_{\mathrm{RO}}(\vec{r}) = 0$ otherwise. This expression replaces the E_{RO} defined in Eq. (6) for the Gaussian case. We can then obtain the scattered field using the "rectangular" version of Eq. (11). This results in

$$E_{\mathrm{rect}}(t) \propto \alpha\beta L E_{\mathrm{RO}}(\vec{0})\rho_0 \mathrm{sinc}(\kappa\alpha) + \frac{1}{2}\alpha\beta L E_{\mathrm{RO}}(\vec{0})\rho_{\mathrm{A}} e^{-\kappa^2 Dt}\left[\mathrm{erf}\left(\beta/\sqrt{4Dt}\right) - \frac{\sqrt{4Dt}}{\beta\sqrt{\pi}}\left(1 - e^{-\beta^2/4Dt}\right)\right]$$
$$\times\left[-\frac{2}{\sqrt{\pi}}e^{\kappa^2 Dt}\left(1 - e^{-\alpha^2/(4Dt)}\cos(\kappa\alpha)\right)\sqrt{\frac{Dt}{\alpha^2}} - \left(\frac{\cos(\kappa\alpha)}{\kappa\alpha} - 2\kappa\alpha\frac{Dt}{\alpha^2}\right)\mathrm{erfi}\left(\kappa\sqrt{Dt}\right)\right.$$
$$\left. + \mathrm{Re}\left\{\left(1 + 2i\kappa\alpha\frac{Dt}{\alpha^2} - i\frac{e^{i\kappa\alpha}}{\kappa\alpha}\right)\mathrm{erf}\left(\frac{\alpha}{\sqrt{4Dt}} + i\kappa\sqrt{Dt}\right)\right\}\right], \tag{20}$$

where the imaginary error function $\mathrm{erfi}(z) = \mathrm{erf}(iz)/i$ and is real-valued for real arguments. The result in Eq. (20) amounts to a slight difference from Eq. (21) in Ref. [21], as shown in Fig. 8. Here, we show the decay curves predicted by Eq. (20), Eq. (21) in Ref. [21], and Eq. (5) on a log scale. The discernible differences between the predictions of Eq. (20) and Eq. (21) in Ref. [21], however, result in corrected diffusion values that agree within the error bars quoted in Ref. [21].

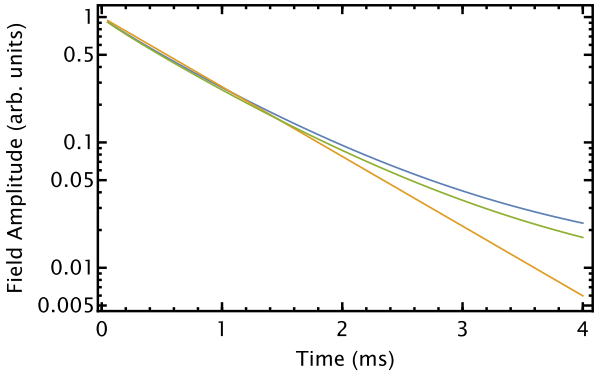


Fig. 8. Comparison of the scattered electric field as described by Eq. (12) (green), Eq. (21) from Ref. [21] (blue), and the plane-wave solution Eq. (5) (orange). Curves are shown with a log vertical scale.

We see that for early times with $Dt \ll \alpha^2$ and $Dt \ll \beta^2$, Eq. (20), with a negligible contribution from the term proportional to ρ_0, leads to

$$E_{\mathrm{rect}}(t) \propto \frac{1}{2}\alpha\beta L E_{\mathrm{RO}}(\vec{0})\rho_{\mathrm{A}} e^{-\kappa^2 Dt}\left(1 - \frac{2}{\sqrt{\pi}}\sqrt{\frac{Dt}{\beta^2}}\right)$$
$$\times\left[d_0 + d_1\sqrt{\frac{Dt}{\alpha^2}} + d_3\left(\frac{Dt}{\alpha^2}\right)^{3/2} + d_5\left(\frac{Dt}{\alpha^2}\right)^{5/2} + O\left(\left(\frac{Dt}{\alpha^2}\right)^3\right)\right] \tag{21}$$

with

$$d_0 = 1 + \frac{\sin(\kappa\alpha)}{\kappa\alpha}, \tag{22}$$

$$d_1 = -\frac{2}{\sqrt{\pi}}\left(1 + \cos(\kappa\alpha)\right), \tag{23}$$

$$d_3 = \frac{2}{\sqrt{\pi}}(\kappa\alpha)^2\left(1 - \frac{1}{3}\cos(\kappa\alpha)\right), \tag{24}$$

$$d_5 = \frac{1}{3\sqrt{\pi}}(\kappa\alpha)^4\left(1 - \frac{3}{5}\cos(\kappa\alpha)\right). \tag{25}$$

Hence, the early time behavior of $E_{\mathrm{rect}}(t)$ is nonanalytic in time, which, as we will show next, leads to significant deviations from the ideal exponential behavior observed for models assuming plane-wave and Gaussian laser beam profiles.

In Fig. 9, we show the ratio of Eqs. (20) and (5) in green, and the ratio of the non-analytic approximation shown in Eqs. (21) and (5) in orange over the same time interval as for the Gaussian model of transit time corrections. We see that the rectangular model described by Eq. (20) leads to a deviation from the plane-wave case that reaches nearly 300% at the largest timescale.

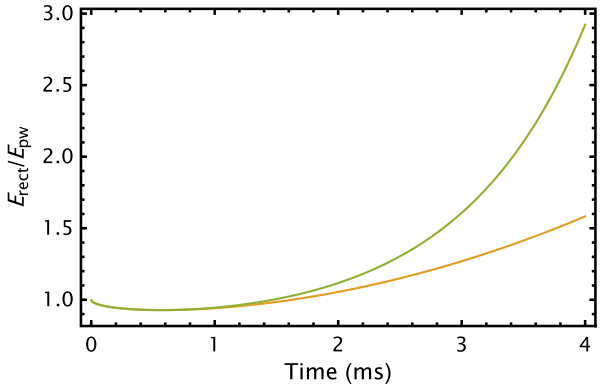


Fig. 9. Ratio of scattered electric fields from the rectangular distribution with a rectangular readout profile, E_R, and the plane-wave distribution, E_{pw}, as a function of time (green). Ratio of the non-analytic approximation in Eq. (21) and the plane-wave distribution, E_{pw} (orange). The electric fields have been normalized to have the same value at $t = 0$ and system parameters are those used in Fig. 7.

This contrasts with the Gaussian case shown in Fig. 5 with similar system parameters. The Gaussian model predicts a ratio close to one over the same time interval. The impact of these differences can be seen in Table 2 of Ref. [21]. Since the approximation given by Eq. (21) is significantly different from the predictions of Eq. (20), we do not use it further.

The rectangular and Gaussian models are relatively insensitive to changes in the geometric parameters α, β, and a, b respectively, such that a 10% variation in these parameters results in a variation of 1% or less in the corrected value of D. Nonetheless, the error in the geometric parameters is propagated to the final results reported in Ref. [21]. We note that the rectangular model gives a larger correction to the diffusion values than the Gaussian model. We now discuss the implications of this larger correction. In Ref. [21], we use the weighted averages of the corrections predicted by the Gaussian and the rectangular models. We reported an error bar in diffusion that was computed as the quadrature sum of (i) the error in the rectangular model, (ii) the error in the Gaussian model, and (iii) half the difference between the corrected values given by these two models. This procedure ensures that the error bar encompasses the full range of corrections predicted by either model. Ongoing experiments [29] will minimize the error in the transit-time correction by using spatial filters to produce larger Gaussian profiles. Therefore, the rectangular model produces a larger transit-time correction and, as a result, reduces the accuracy of the corrected diffusion coefficients. Nevertheless, the corrections predicted by Eq. (21) of Ref. [21] and Eq. (20) are the same within error, as discussed in the context of Fig. 8.

6. CONCLUSION

We have outlined the effects of transit-time corrections on measurements of diffusion coefficients of trace amounts of Rb vapor in inert gases. Although we have presented improved models for the Gaussian and rectangular cases, these improvements do not significantly impact the corrections to diffusion coefficients based on the calculations presented in Ref. [21]. These models will support future experimental work to reduce the impact of transit time effects. As described in Refs. [20,21], measurements of these diffusion coefficients can be used to realize a quantum pressure sensor for the calibration of pressure gauges if the accuracy of these determinations can reach the level of 0.5%. Transit time corrections are also of interest to a wider class of diffusion experiments that rely on optical pumping [15–19].

Funding. Canada Foundation for Innovation); Ontario Centre of Innovation); Ontario Innovation Trust); Natural Sciences and Engineering Research Council of Canada); Helen Freedhoff Memorial Fund).

Disclosures. The authors declare no conflicts of interest.

Data availability. Data underlying the results presented in this paper are not publicly available at this time but may be obtained from the authors upon reasonable request.

REFERENCES

1. J. L. Cohen and P. R. Berman, "Transit-time effects in coherent transient spectroscopy," Phys. Rev. A **54**, 5262–5274 (1996).
2. V. Shukla and A. Ray, "Experimental study on transit time broadening in rubidium 5S-5D excitation," Appl. Opt. **61**, 4719–4724 (2022).
3. J. C. Bergquist, "13-Doppler-free spectroscopy," in *Atomic, Molecular, and Optical Physics: Atoms and Molecules*, Vol. **29** of Experimental Methods in the Physical Sciences, F. Dunning and R. G. Hulet, eds. (Academic, 1996), pp. 255–272.
4. M. Levenson, *Introduction to Nonlinear Laser Spectroscopy* (Academic, 2012).
5. M. Bruvelis, J. Ulmanis, N. Bezuglov, *et al.*, "Analytical model of transit time broadening for two-photon excitation in a three-level ladder and its experimental validation," Phys. Rev. A **86**, 012501 (2012).
6. J. E. Thomas and R. A. Forber, "Transverse atomic motion in transient polarization phenomena," Opt. Lett. **9**, 56–58 (1984).
7. I. Yavin, M. Weel, A. Andreyuk, *et al.*, "A calculation of the time-of-flight distribution of trapped atoms," Am. J. Phys. **70**, 149–152 (2002).
8. I. Yavin, T. Mikaelian, and A. Kumarakrishnan, "Calculation of the transfer efficiency between dual magneto-optical traps and simulation of a ioffe trap for Bose Einstein condensation," Can. J. Phys. **81**, 651–661 (2003).
9. B. Barrett, A. Carew, S. Beattie, *et al.*, "Measuring the atomic recoil frequency using a modified grating-echo atom interferometer," Phys. Rev. A **87**, 033626 (2013).
10. C. Mok, B. Barrett, A. Carew, *et al.*, "Demonstration of improved sensitivity of echo interferometers to gravitational acceleration," Phys. Rev. A **88**, 023614 (2013).
11. G. Carlse, J. Randhawa, A. Pouliot, *et al.*, "Gravitational sensing in the frequency domain using an echo atom interferometer," Phys. Rev. A **112**, L061302 (2025).
12. B. Barrett, I. Chan, and A. Kumarakrishnan, "Atom-interferometric techniques for measuring uniform magnetic field gradients and gravitational acceleration," Phys. Rev. A **84**, 063623 (2011).
13. I. Chan, A. Andreyuk, S. Beattie, *et al.*, "Properties of magnetic sublevel coherences for precision measurements," Phys. Rev. A **78**, 033418 (2008).
14. G. Carlse, J. Randhawa, E. Ramos, *et al.*, "Velocimetry using free-induction decay of matter-wave lattices," Phys. Rev. A **111**, L021304 (2025).
15. M. A. Bouchiat, J. Brossel, and L. C. Pottier, "Evidence for Rb-rare-gas molecules from the relaxation of polarized Rb atoms in a rare gas. Experimental results," J. Chem. Phys. **56**, 3703–3714 (1972).
16. X. Zeng, Z. Wu, T. Call, *et al.*, "Experimental determination of the rate constants for spin exchange between optically pumped K, Rb, and Cs atoms and ^{129}Xe nuclei in alkali-metal–noble-gas van der Waals molecules," Phys. Rev. A **31**, 260–278 (1985).
17. T. G. Walker and W. Happer, "Spin-exchange optical pumping of noble-gas nuclei," Rev. Mod. Phys. **69**, 629–642 (1997).
18. G. D. Cates, R. J. Fitzgerald, A. S. Barton, *et al.*, "Rb-^{129}Xe spin-exchange rates due to binary and three-body collisions at high Xe pressures," Phys. Rev. A **45**, 4631–4639 (1992).

19. R. Chrapkiewicz, W. Wasilewski, and C. Radzewicz, "How to measure diffusional decoherence in multimode rubidium vapor memories?" Opt. Commun. **317**, 1–6 (2014).
20. A. Pouliot, G. Carlse, H. C. Beica, *et al.*, "Accurate determination of an alkali-vapor–inert-gas diffusion coefficient using coherent transient emission from a density grating," Phys. Rev. A **103**, 023112 (2021).
21. A. Pouliot, E. C. Ramos, G. Carlse, *et al.*, "Measurements of diffusion coefficients for rubidium–inert-gas mixtures using coherent scattering from optically pumped population gratings," Phys. Rev. A **111**, 033108 (2025).
22. A. Pouliot, G. Carlse, H. C. Beica, *et al.*, "Erratum: Accurate determination of an alkali-vapor-inert-gas diffusion coefficient using coherent transient emission from a density grating [Phys. Rev. A 103, 023112 (2021)]," Phys. Rev. A **111**, 039903 (2025).
23. P. R. Berman, "Collisional decay and revival of the grating stimulated echo," Phys. Rev. A **49**, 2922–2932 (1994).
24. B. Dubetsky and P. R. Berman, "Magnetic grating free induction decay and magnetic grating echo," Laser Phys. **4**, 1017–1029 (1994).
25. A. Pouliot, "Measurements of diffusion coefficients for rubidium atoms in inert gas mixtures using coherent scattering from optically pumped population gratings," PhD dissertation (York University, 2025).
26. P. R. Berman, G. Rogers, and B. Dubetsky, "Rate equations between electronic-state manifolds," Phys. Rev. A **48**, 1506–1513 (1993).
27. W. J. Olver, A. B. Daalhuis, D. W. Lozier, *et al.*, eds. *NIST Digital Library of Mathematical Functions* (National Institute of Standards and Technology, 2025).
28. E. W. Ng and M. Geller, "A table of integrals of the error functions," J. Res. Natl. Bureau Stand. Math. Sci. **73B**, 1 (1969).
29. E. C. Ramos, A. Pouliot, G. Carlse, *et al.*, "Temperature and pressure dependence of diffusion coefficients of Rb-inert gas mixtures using coherent scattering from optically pumped population gratings," in *Proceedings of SPIE Quantum West* (2026), paper 13914-1.